Hindawi
Advances in Civil Engineering
Volume 2019, Article ID 7358710, 15 pages
https://doi.org/10.1155/2019/7358710

Research Article

Evaluation of 3D Nonlinear Earthquake Behaviour of the Ilısu CFR Dam under Far-Fault Ground Motions

Memduh Karalar and Murat Çavuşli

Bulent Ecevit University, Department of Civil Engineering, Zonguldak, Turkey

Correspondence should be addressed to Memduh Karalar; memduhkaralar@gmail.com

Received 7 August 2018; Revised 27 September 2018; Accepted 19 December 2018; Published 8 January 2019

Academic Editor: Geoffrey W. Rodgers

In the recent times, many huge concrete face rockfill dams (CFRDs) have been modelled and constructed in the world, and many of these dams are located on the strong earthquake zones. Examination of the seismic behaviour of a CFR dam built on the seismic zone is very important to assess the safety and future of the dam. For this reason, the nonlinear earthquake behaviour of these dams should be constantly observed taking into account the seismicity of the zone. In this study, three-dimensional (3D) seismic behaviour of the Ilısu dam built on the East Anatolian Fault (EAF) line is examined considering the effect of the important various far-fault earthquakes. The 3D finite difference model of the Ilısu dam is created using the FLAC3D software based on the finite difference method. The dam body, foundation, and concrete slab constantly interact during the lifetime of the CFRDs. Therefore, the special interface elements are defined between the dam body, concrete slab, and foundation to represent the interaction condition. The Mohr–Coulomb nonlinear material model is used for the rockfill materials and foundation. Moreover, the concrete slab is modelled considering the Drucker–Prager nonlinear material model to represent the nonlinearity of the concrete. Very special seismic boundary conditions rarely used for CFR dams in the past are used in this work. These boundary conditions are free-field and quiet boundary conditions. The free-field boundary condition that is a very important boundary condition for the nonlinear seismic analyses is considered for the lateral boundaries of the 3D model. In addition, the quiet artificial boundary condition is used for the bottom of the foundation. While defining these boundary conditions, the special fish functions are created and defined to the software. Moreover, the hysteric damping coefficients are separately calculated for all of the materials. These special damping values are defined to the FLAC3D software using the special fish functions to capture the effects of the variation of the modulus and damping ratio with the dynamic shear-strain magnitude. In the numerical analyses, a total of 7 various strong far-fault earthquakes are used for the 3D nonlinear earthquake analyses, and 7 different numerical analyses are performed for the full-reservoir condition of the Ilısu CFR dam. According to the seismic results, the principal stresses for the three critical nodal points on the dam body surface are examined and evaluated in detail. It is clearly understood that the nonlinear seismic behaviour of the Ilısu dam changes depending on the magnitudes and periods of the far-fault earthquakes. Each far-fault earthquake has different seismic effects on the nonlinear principal stress behaviour of the Ilısu CFR dam.

1. Introduction

In the past, dams very important water structures were constructed for only irrigation. When civilizations developed, there was a greater need for water supply, irrigation, flood control, navigation, water quality, sediment control, and energy. Because of this reason, these critical structures are constructed for specific aims such as water supply, flood control, irrigation, navigation, sedimentation control, and hydropower. In the world, there are many dam types, and concrete faced rockfill (CFR) dams are one of these dam types. Today, many huge CFR dams are constructed, and sometimes they have to be built on the seismic zones where seismic activities intensively occur. Thus, these structures may expose the large earthquake loads. This situation can be dangerous for the safety of people who live around these dams. For this reason, the seismic behaviour of these structures should be constantly observed, and seismic safety of them is evaluated in detail.

When two different tectonic plates come into contact with each other, earthquakes suddenly take place. Afterwards,

the surface of the Earth abruptly shakes with sudden release of energy in the elastic upper crust and the Earth randomly moves in all directions (x, y, and z directions). So, all of the aspects of the strong ground motions have to take into account for monitoring of the CFR dam's safety [1]. The near-fault and far-fault earthquakes have various seismic effects on the nonlinear behaviour of the CFR dams. Characteristic properties of these seismic ground motions were initially observed by Hudson [2] and Housner and Trifunac [3]. It was clearly indicated that the ground motions which are about 20 km distance from the fault rupture are accepted as near-fault seismic ground motions. It was also stated that the effects of the far-fault earthquakes and near-fault earthquakes on the seismic behaviour of the structures are very different from each other. The effect of near-fault earthquakes on the seismic behaviour of the CFR dams was examined by many investigators. But, very few investigators have investigated the effect of the far-fault earthquakes on the nonlinear seismic behaviour of the CFR dams. In 1933, Westergaard [4] presented very important results about the effect of the earthquakes on the dam-foundation-reservoir interaction. The importance of the hydrodynamic loads on the nonlinear behaviour of the dam body during earthquake is clearly indicated. In 1966, Chopra [5] revealed the effect of water compressibility on the hydrodynamic pressure for the strong ground motions. This result is very important for the design of dams. Arici [6] investigated the seismic performance of a CFR, and it was indicated that earthquake loads give rise to the strong cracks on the concrete slab. Moreover, performance analyses of concrete slab showed that the reinforcement ratio in the concrete slab is the most effective countermeasure to diminish the disaster during strong seismic loads. Yang and Chi [7] developed a method to evaluate the earthquake stability of the concrete face rockfill dams. Andrianopoulos et al. [8] revealed that the predominant period of vibration for a CFR dam is highly affected with the input of the ground motion characteristics and its height. In addition, the peak acceleration for the CFR dam's crest is managed with the input motion characteristics, foundation stiffness, and its height. Xu et al. [9] developed nonlinear seismic analysis procedure for the CFR dams taking into account the plastic-damage constitutive model, and it was proposed that this procedure could be adopted into the interaction condition between the foundation and concrete. This procedure is pioneer for modelling of the CFR dams. Cen et al. [10] developed a damage model (the concrete random mesoscopic) to assess the seismic behaviour of the CFR dam's concrete slab. Han et al. [11] examined the earthquake behaviour of the CFR dams considering the finite element method. This work showed that the vertical acceleration for CFR dam's nonlinear response is highly influenced with the rockfill material's permeability. In addition, the study indicated that the settlements of the dam crest can be considerably underestimated by ignoring the strong vertical ground motion. Zou et al. [12] selected 16 different ground motions which include 8 pulse-like earthquakes and 8 non-pulse ground motions for the seismic analyses. The seismic analyses indicated that the ground motion has a significant effect on acceleration of the dam, and it has very important effects on the concrete slab damage and CFR dam's residual deformation. Yazdani and Alembagheri [13] assessed earthquake of a CFR dams constructed on the seismic zone. The interaction system between the dam-reservoir was examined considering the selected pulse-like and nonpulse-like records, and it was indicated that the characteristics of earthquake that is different from pulse nature may manage the seismic responses. Moreover, it was indicated that the nonlinear displacement responses for the fundamental period are the best options under the strong ground motion records with and without pulse nature for the earthquake vulnerability of the dam-reservoir interaction system. In addition, many investigators examined the nonlinear seismic behaviour of the CFR rockfill dams, and the effect of the strong ground motions was discussed in detail [9, 14–24].

Both far-fault and near-fault earthquakes can cause major damages in the CFR dam body. When investigated the literature, it is clearly seen that there are many studies associated with the effect of the near-fault earthquakes on the seismic behaviour of the dams. However, very few investigators examined the effects of the far-fault earthquakes on the nonlinear seismic behaviour of the CFR dams. For this reason, 7 different far-fault ground motions are used in the seismic analyses for the full reservoir condition of the dam in this study, and 7 various numerical analyses are performed and compared with each other. So, this study is very important to evaluate the effect of the different far-fault earthquakes on the fatigue and deterioration of the rockfill materials. Moreover, free-field and quiet seismic boundary conditions rarely used in the past to examine 3D behaviour of the CFR dams are taken into account to examine the 3D nonlinear seismic behaviour of Ilısu CFR dams. Thus, this study is very important for filling these deficiencies in the literature. According to the 3D finite difference analyses, principal stresses are assessed for the seismic analyses. The deteriorations and fatigues in the rockfill materials are evaluated considering the effect of the magnitudes and periods of the far-fault earthquakes.

2. General Descriptions of the Ilısu Hydraulic Project

2.1. Project Location and Geology. The Ilısu dam was completed in 2017, and the project area is 117 km away from the center of Mardin province. The dam was built on the strong seismic zone in Turkey, and it is part of the Southeastern Anatolian Project (GAP). This structure is the largest hydropower project in Turkey, and it is the longest concrete-faced rockfill dam (1775 m) in the world (Figure 1).

The project includes totally 44 million m^3 filling material, 3 diversion tunnels with a diameter of 12 m and length of 1 km, and 3 power tunnels with a diameter of 11 m. The dam's precipitation area is 35509 km^2. The crest width is 8 m and dam body height is 130 m. The lake volume is 10.4 billion m^3. Maximum water elevation is 526.82 m, and reservoir area is 318.5 km^2. The project generates 3.833 GWh power per year in average with an installed capacity of 1.200 MW. The Ilısu dam's location is shown in detail in Figure 1. The slopes of the upstream side and downstream side of the Ilısu dam are 1 : 1.4 and slopes of the transition zones are 2 : 1.5. The typical

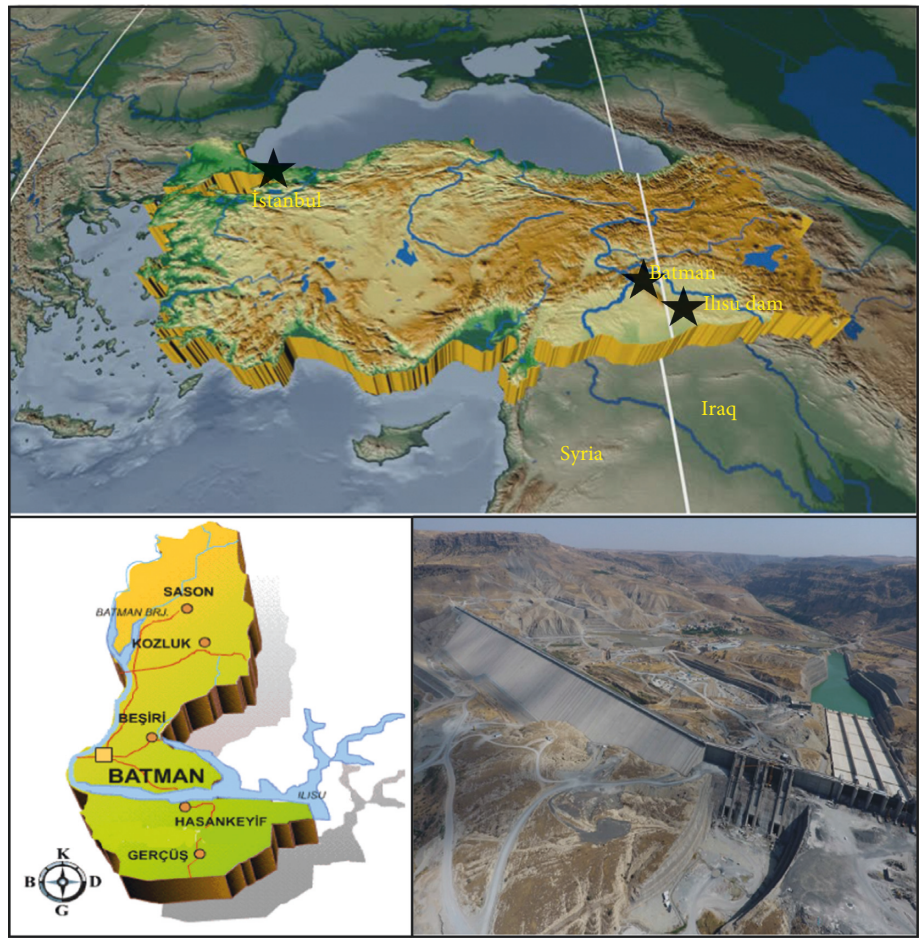

Figure 1: General view of the Ilısu dam [25].

cross section of the Ilısu dam and details of the dam body height are demonstrated in Figure 2. Moreover, geology of Ilısu hydraulic project is shown in Figure 3. According to Figure 3, there are 6 various rockfill materials around the dam project zone. These rockfill materials are limestone, clayey/marley limestone, siltstone/claystone, sandstone/marl, marly/limestone, and basalt. These rockfill materials are used while constructing the body of the Ilısu dam.

2.2. Theoretical Background of the Interaction between Discrete Surfaces. Interaction condition is very critical for huge water structures such as CFR dams. This situation occurs between the dam body, foundation, and concrete slab for the CFR dams. In the FLAC3D software, the interaction condition is represented defining the interaction stiffness values between the discrete surfaces as shown in Figures 4 and 5.

FLAC3D utilizes a special contact logic used in different element methods to represent interaction condition for either side of the interface. As seen in Figure 4, the grid point N is controlled for the contact situation between the grid points M and P. If this contact condition is realized, the normal vector (n) is computed for the grid point N. In addition, the length (L) for the contact at the point N along the interface is described. L represents the half of the nearest grid point's distance to the grid point N. In this method, the interface is divided into contiguous segments, and each segment is checked by a grid point. For time step, the velocity ($\dot{u}_i$) of grid points is stated as seen at equal 1. Since the velocity's unit is displacement for time step and the calculation of the time step is scaled to unity to speed convergence the displacement for each time step is

$$\Delta u_i \equiv u_i. \tag{1}$$

A contact point's displacement vector is resolved for the normal and shear directions and total forces (normal and shear) are determined as follows:

$$\begin{aligned} F_{\mathrm{n}}^{(t+\Delta t)} &= F_{\mathrm{n}}^{(t)} - k_{\mathrm{n}} \Delta u_{\mathrm{n}}^{(t+(1/2)\Delta t)} L, \\ F_{\mathrm{s}}^{(t+\Delta t)} &= F_{\mathrm{s}}^{(t)} - k_{\mathrm{s}} \Delta u_{\mathrm{s}}^{(t+(1/2)\Delta t)} L. \end{aligned} \tag{2}$$

Normal (k_{n}) and shear (k_{s}) stiffness values are very different for each interface surface. Unit of the k_{n} and k_{s} stiffness is stress/displacement [26]. In this study, k_{n} and k_{s} stiffness are separately calculated for each discrete surface. These stiffness values are considered as 10^8 Pa/m between the dam body and foundation. Moreover, these values are taken into account as 10^9 Pa/m between the dam body and concrete slab [27]. Shear and normal stiffness values are defined to the FLAC3D software using special fish functions.

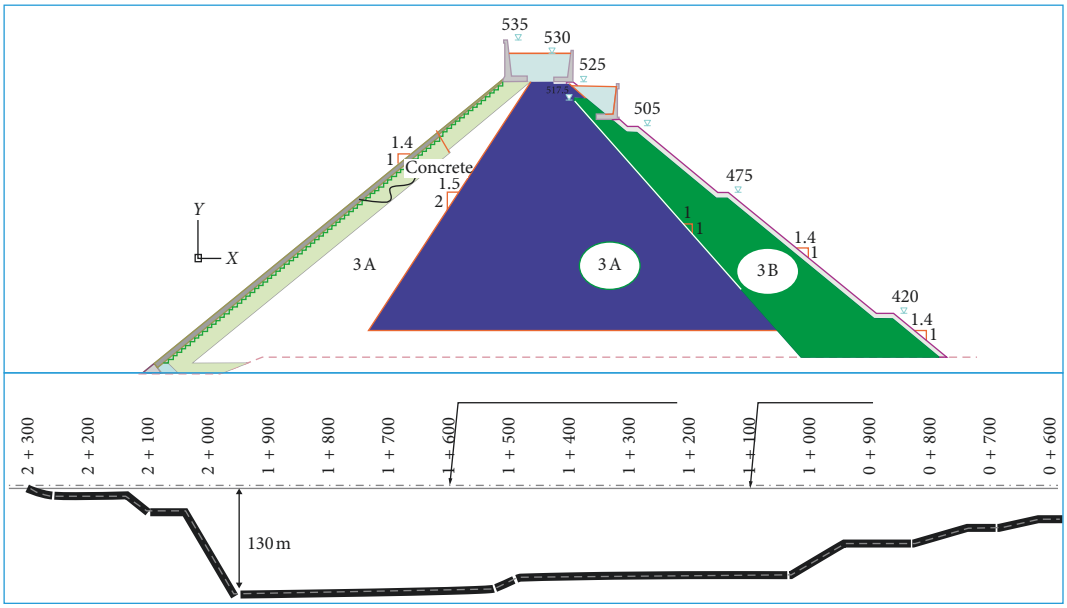

Figure 2: (a) The typical cross section of the Ilısu dam. (b) Changing of the dam body depth along crest axis [25].

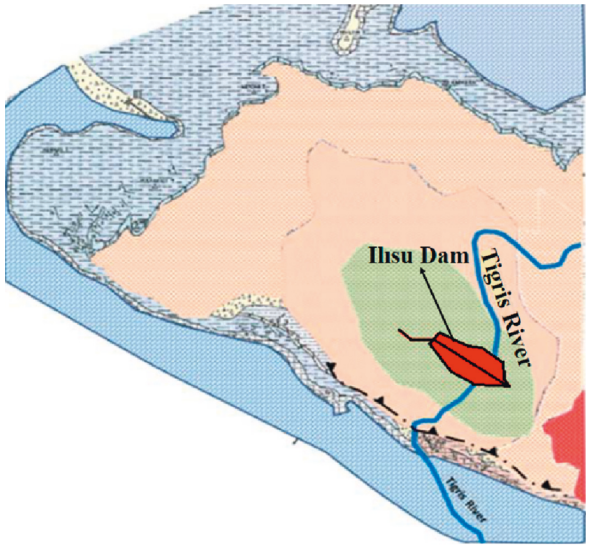

Figure 3: Geology of the Ilısu hydraulic project.

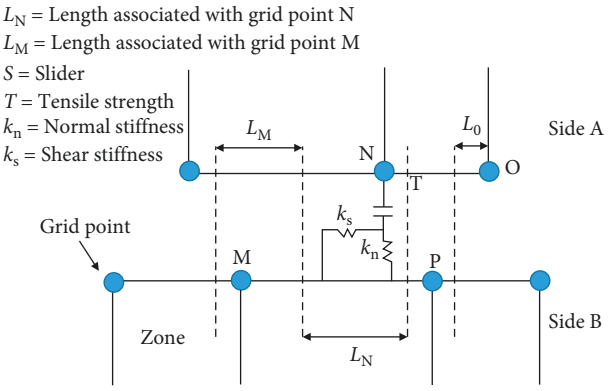

Figure 4: An interface condition between A and B sides.

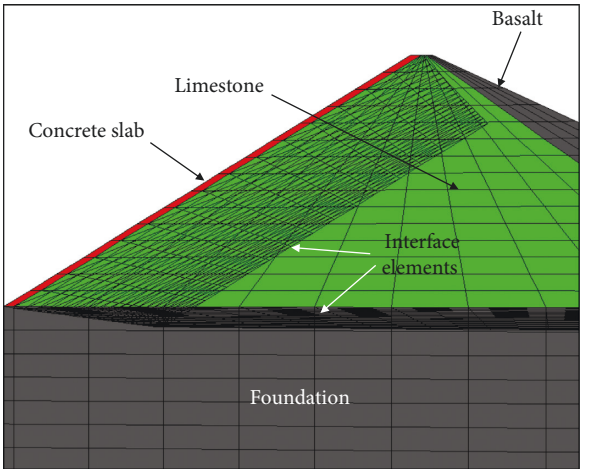

Figure 5: Interface conditions between the dam body-foundation and dam body-concrete slab of the Ilısu dam.

Normal and shear stiffness (k_n and k_s) are not well-known parameters, and they are not easily calculated. Many numerical procedures have been derived in the past, and two important methods are generally used in the interaction analyses. One of them is based on the rock mass's deformation properties, and second one is derived from the joint infilling material's properties. These procedures are explained in detail as described below.

2.3. Calculation of Normal and Shear Stiffness considering Rockfill Properties

$$\frac{1}{E_{\mathrm{m}}} = \frac{1}{E_{\mathrm{i}}} + \frac{1}{k_{\mathrm{n}} L}. \tag{3}$$

In equation (3), E_{m} is the modulus of rock mass; E_{i} is intact rock modulus; k_{n} is the joint normal stiffness; and L is mean joint spacing. Equation (3) can be rearranged to obtain the joint normal stiffness as given in

$$k_{\mathrm{n}} = \frac{E_{\mathrm{i}} E_{\mathrm{m}}}{L\left(E_{\mathrm{i}} - E_{\mathrm{m}}\right)}. \tag{4}$$

The same expression may be considered to derive a relation for the joint shear stiffness as seen at

$$k_{\mathrm{s}} = \frac{G_{\mathrm{i}} G_{\mathrm{m}}}{L\left(G_{\mathrm{i}} - G_{\mathrm{m}}\right)}. \tag{5}$$

In equation (5), G_{m} is the rock mass shear modulus; G_{i} is intact rock shear modulus; and k_{s} is the joint shear stiffness. When the equivalent continuum assumption is extended to three orthogonal joint sets, it is obtained the following relations:

$$\begin{aligned} E_{\mathrm{a}} &= \left(\frac{1}{E_{\mathrm{i}}} + \frac{1}{L_{\mathrm{a}} k_{\mathrm{na}}}\right)^{-1}, \quad (a = 1, 2, 3), \\ G_{\mathrm{ab}} &= \left(\frac{1}{G_{\mathrm{i}}} + \frac{1}{L_{\mathrm{a}} k_{\mathrm{sa}}} + \frac{1}{L_{\mathrm{b}} k_{\mathrm{sb}}}\right)^{-1}, \quad (a, b = 1, 2, 3). \end{aligned} \tag{6}$$

Many equals have been acquired for 2D and 3D characterizations.

2.4. Calculation of Normal and Shear Stiffnesses considering Joint Infill Materials. Second procedure for forecasting the stiffness of joint presumes that an interaction joint has an infill material. The joint stiffness can be evaluated from the infilling material by the following equation:

$$\begin{aligned} k_{\mathrm{n}} &= \frac{E_0}{h}, \\ k_{\mathrm{s}} &= \frac{G_0}{h}. \end{aligned} \tag{7}$$

In equation (7), k_{s} is joint shear stiffness; k_{n} is joint normal stiffness; G_{o} is the shear modulus of infill material; and E_{o} is Young's modulus of infill material; and h is joint thickness or opening.

2.5. Mohr–Coulomb Material Model. This nonlinear material model is generally used for many rockfill materials in the FLAC3D software. The implementation of Mohr–Coulomb material model is given as following: $\sigma_1, \sigma_2, \sigma_3$ are utilized for the out of plane stress. The principal directions and principal stresses are assessed from the components of stress tensor.

$$\sigma_1 \le \sigma_2 \le \sigma_3, \tag{8}$$

$\Delta e_1, \Delta e_2, \Delta e_3$ are defined as seen below:

$$\Delta e_i = \Delta e_i^e + \Delta e_i^p, \quad i = 1.3. \tag{9}$$

In equation (9), e and p are the elastic part and plastic part. The plastic parts are nonzero only during plastic flow [26]. Hooke's law for principal stress and principal strain is as seen below;

$$\begin{aligned} \Delta\sigma_1 &= \alpha_1 \Delta e_1^{\mathrm{e}} + \alpha_2 \left(\Delta e_2^{\mathrm{e}} + \Delta e_3^{\mathrm{e}}\right), \\ \Delta\sigma_2 &= \alpha_1 \Delta e_2^{\mathrm{e}} + \alpha_2 \left(\Delta e_1^{\mathrm{e}} + \Delta e_3^{\mathrm{e}}\right), \\ \Delta\sigma_3 &= \alpha_1 \Delta e_3^{\mathrm{e}} + \alpha_2 \left(\Delta e_1^{\mathrm{e}} + \Delta e_2^{\mathrm{e}}\right), \end{aligned} \tag{10}$$

where $\alpha_1 = K + 4G/3$ and $\alpha_2 = K - 2G/3$.

Potential and yield functions are presented in detail as given below.

According to equation (11), the failure criterion can be defined in the plane as seen in Figure 6. The failure envelope is considered from point A to B:

$$f^{\mathrm{s}} = \sigma_1 - \sigma_3 N\phi + 2c\sqrt{N\phi}, \tag{11}$$

and from point B to C by a tension yield function

$$f^{\mathrm{t}} = \sigma^{\mathrm{t}} - \sigma_3. \tag{12}$$

In equations (11) and (12), c is the cohesion, ϕ is the friction angle, and σ_{t} is the tensile strength and

$$\begin{aligned} N\phi &= \frac{1 + \sin\phi}{1 - \sin\phi}, \\ \sigma_{\max}^{\mathrm{t}} &= \frac{c}{\tan\phi}, \end{aligned} \tag{13}$$

and g^{s} (the shear potential function) represents a flow rule:

$$g^{\mathrm{s}} = \sigma_1 - \sigma_3 N_\psi. \tag{14}$$

In equation (14), ψ is the dilation angle:

$$N_\psi = \frac{1 + \sin\psi}{1 - \sin\psi}. \tag{15}$$

The flow rule that associates of tensile failure is derived from the potential function g^{t}

$$g^{\mathrm{t}} = -\sigma_3. \tag{16}$$

The flow rules for 3D dam model described a unique definition in the vicinity of an edge of the composite yield function in three-dimensional stress space by application of a technique, illustrated below, for the case of a shear-tension edge. A function, $h(\sigma_1, \sigma_3) = 0$, which is represented by the diagonal between the representation of $f^{\mathrm{s}} = 0$ and $f^{\mathrm{t}} = 0$ in the (σ_1, σ_3) plane, is defined in Figure 7. This function has the form

$$h = \sigma_3 - \sigma^{\mathrm{t}} + \alpha^{\mathrm{p}} \left(\sigma_1 - \sigma^{\mathrm{p}}\right). \tag{17}$$

In equation (17), α^{p} and σ^{p} are defined as below:

$$\begin{aligned} \alpha^{\mathrm{p}} &= \sqrt{1 + N_\phi^2} + N_\phi, \\ \sigma^{\mathrm{p}} &= \sigma^{\mathrm{t}} N_\phi - 2c\sqrt{N_\phi}. \end{aligned} \tag{18}$$

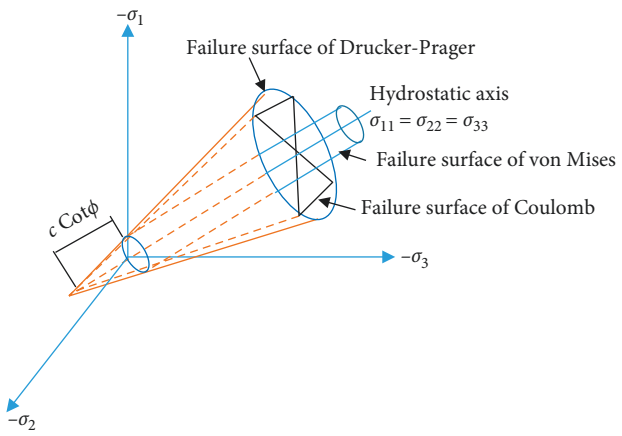

Figure 6: Mohr–Coulomb failure criterion [26].

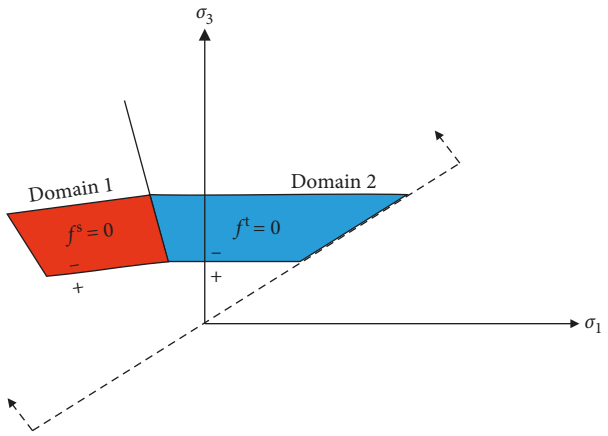

Figure 7: Mohr–Coulomb model: domains used in the definition of the flow rule [26].

3. Finite Difference Model and Material Properties of Ilısu Dam

While creating the 3D finite difference model of Ilısu dam, all rockfill materials and concrete slab built to hinder the leakage in the dam body are modelled as the original project of the dam. The 3D model of the dam body has 5 different sections, and these sections' geometrical properties are very different from each other. Each section has different heights along the dam body. While modelling the Ilısu dam, these different sections are merged, and the dam body's finite difference model is created. The Ilısu dam body's 3D finite difference model of has 4 various blocks. Details of the sections and blocks are presented in Figure 8.

After the three-dimensional model of the dam body is modelled, the foundation and reservoir water are created in detail. While modelling the foundation, foundation is extended toward downstream, and the valley side as much as the dam's height. Also, it is extended three times of the dam height at upstream side of the dam. Finally, foundation's height is taken into account as much as the dam's height. These lengths and heights are the most critical

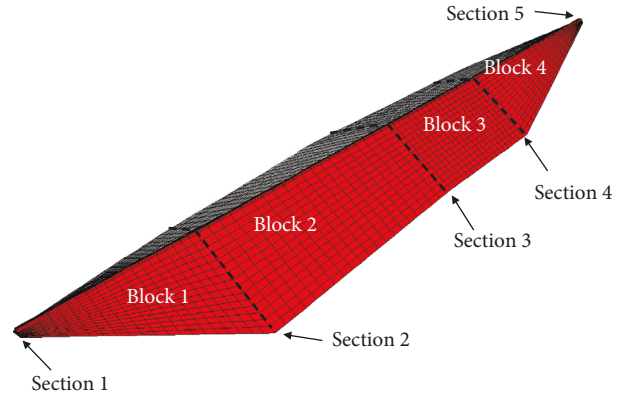

Figure 8: View of the section and blocks in the 3D finite difference model.

conditions for the seismic analyses of the dams [28]. Totally 1104547 finite difference elements are used in the 3D finite difference model. The Mohr–Coulomb material model and Drucker–Prager material model special nonlinear material models are used for the rockfill material-foundation and concrete slab, respectively. Special fish functions are used while defining the material model to the FLAC3D software. Moreover, special interface elements are defined between the rockfill material-foundation and the concrete slab-rockfill material to provide interaction condition between the discrete surfaces. Hysteretic damping models are generally used to characterize the nonlinear mechanical system's dynamic properties. Various hysteretic damping models are calculated for all materials (rockfill materials, concrete slab, and foundation) because all materials have different characteristic properties. While defining these hysteric damping models to the FLAC3D software, special fish functions are written and defined to the FLAC3D software. Free-field seismic boundary condition that is special boundary condition for earthquake analyses is defined to the lateral boundaries of the 3D finite difference model for seismic analyses. This boundary condition is available for only lateral boundaries as seen Figure 9, and it is made up of a combination of a load history and a viscous boundary. These boundaries allow for an input of an earthquake motion while still absorbing incoming waves. In addition, quiet boundary (viscous boundary) condition is used for the bottom of the 3D model in the nonlinear earthquake analyses. Free-field and quiet boundary conditions for the 3D finite difference model of the Ilısu dam are shown in Figure 10 in detail.

Afterwards, the reservoir water is modelled considering the effect of the leakage in the dam body. Water height is taken into account as empty water condition, 50 m, 100 m, and 130 m, of the reservoir water height, respectively. While creating the reservoir water, water loads are calculated for each node of the dam's upstream side considering hydrostatic ware pressure. Then, water table is defined to the FLAC3D software using the special fish function to provide the leakage condition in the dam body. The creating and meshing of the three-dimensional model of the Ilısu dam took very long time. This process is not automated, and so

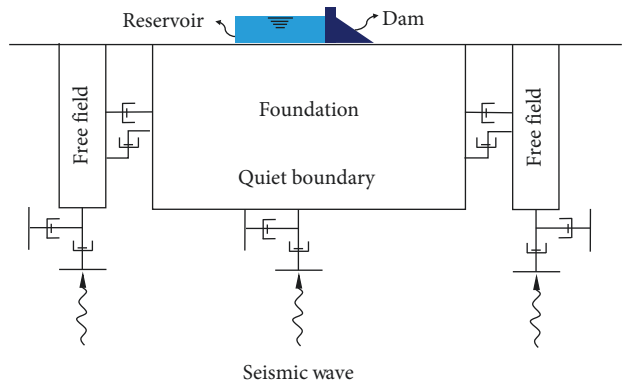

Figure 9: Boundary conditions for the finite difference model.

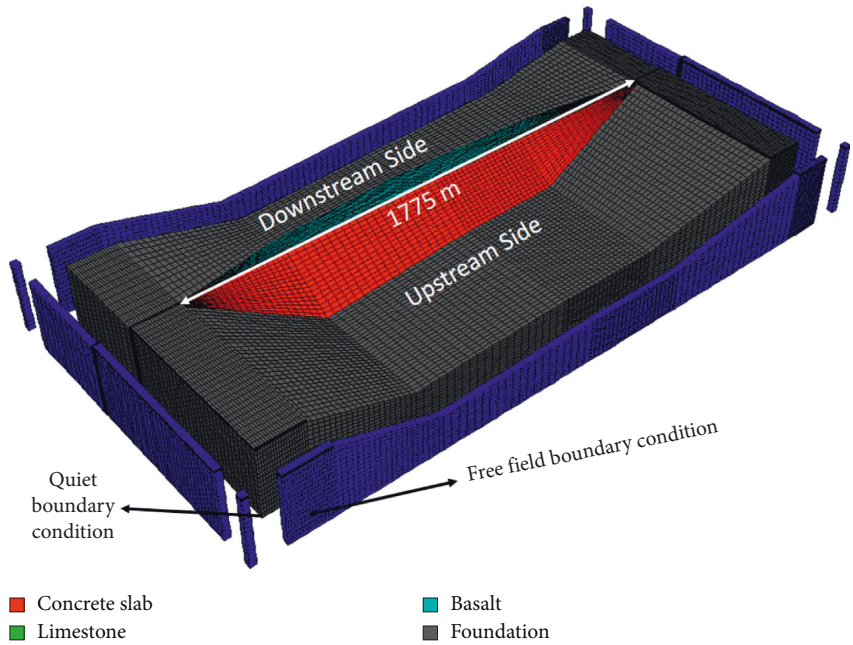

Figure 10: 3D finite difference model of the Ilısu dam.

each process is individually calculated. Many problems and errors are encountered during nonlinear seismic analyses due to the 3D finite difference model of the Ilısu dam has a great number of nodes and elements. So, the 3D mesh is changed many times, and a new mesh is modelled so that the correct result can be achieved and the program will not fail. While analyzing the Ilısu dam, totally 6 different mesh widths are created to find the correct mesh width. These widths are 10 m, 15 m, 20 m, 30 m, 40 m, and 50 m, respectively. It is seen from numerical analyses that the maximum settlements on the crest of the dam do not change for less mesh width than 10 m (Figure 11). So, mesh width is selected 10 m for seismic analyses.

The Ilısu dam was constructed as concrete faced rockfill dam, and it was built using many various rockfill materials such as basalt (3B), limestone (3A), and bedding zone (2B). In addition, all rockfill materials have different mechanical properties. Mechanical properties of the rockfill materials are selected from the laboratory experiments for earthquake

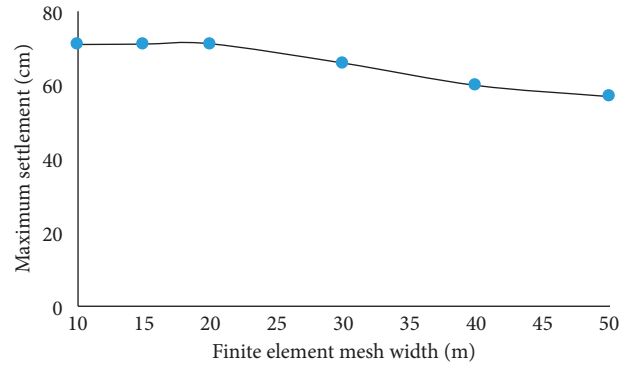

Figure 11: Settlement changes of the crest for different mesh widths.

analyses as given in Table 1. Moreover, while constructing the Ilısu dam, these rockfill materials were compacted by sheepsfoot rollers.

Table 1: Material properties of the Ilısu dam [25].

Characteristics	Specify weight	Unit weight	Porosity	Water content	Air content	Material content
Unit	(g/cm^3)	(g/cm^3)	(%)	(%)	(%)	(%)
2B material	2.74	2.23	18.61	4.05	14.56	81.39
3A material	2.68	1.99	25.75	7.78	17.97	74.25
3B material	3.01	2.25	25.25	1.50	23.75	74.75

4. Geologic Background of Turkey and Ground Motion Inputs

Turkey is one of the most active seismic regions of the world. In Turkey, the tectonic faults depend on the Aegean plate, African plate, Arabian plate, Anatolian plate, Black Sea plate, and Eurasian plate. The neotectonics of Turkey is directed with 3 important plates: (a) the Aegean-Cyprean; (b) the North Anatolian Fault (NAF) zone; and (c) the East Anatolian Fault (EAF) zone (Figure 12). EAF zone is a plate boundary extending over 500 km, and it is located between the Arabian and Anatolian plates. It is currently one of the largest active faults in the world. Plate motions occur by slip rates between 6 and 10 mm/year. In addition, there have been large-magnitude ($M > 7$) earthquakes in the EAF zone. The fault map of Turkey is shown in Figure 12 in detail. Moreover, the Ilısu dam was built very close to the East Anatolian Fault (EAF). Because the EAF zone has a long and extensive historical record, it provides a critical natural laboratory to study earthquake mechanics and fault behaviour. Although the important historical record of Turkey is available, all historical earthquakes records for the East Anatolian Fault zone are not yet available.

In this study, totally 7 different far-fault ground motions are used for the 3D earthquake analyses. These earthquakes occurred at various countries of the world, and they have various durations. Duration of the Borrego Springs earthquake is 42 seconds. For the Northern California and San Fernando earthquakes, it is 15 seconds. Moreover, it is 32, 30, 24, and 28 seconds for Italy, Kobe, Morgan, and Kocaeli earthquakes, respectively. These earthquakes have different magnitudes and accelerogram. In addition, these earthquakes have very different time intervals from each other. Acceleration-time graphics of the far-fault earthquakes are presented in Figure 13.

5. Numerical Results

In the world countries where the strong seismic ground motion occurs, such as Turkey, while constructing the huge water structure (e.g., CFR dams), we can never ignore the seismic characteristics of the zone. For this reason, the examination of the nonlinear seismic behaviour of such structures is vital importance in terms of the safety and future of these water constructions. In this study, the nonlinear earthquake behaviour of the Ilısu dam is investigated graphically in detail. Nonlinear seismic analyses are performed for the full reservoir condition of the Ilısu dam considering various far-fault ground motions. Total 7 various far-fault earthquakes are used in the numerical analyses. The characteristic properties of these earthquakes are different from each other, and the properties of the ground motions are shown in upper section in detail. While performing earthquake analyses for full-reservoir condition of the dam, principal stresses and displacements that occurred from the construction phase of the dam were not ignored. In other words, before performed the seismic analyses, all displacements (vertical and horizontal) and principal stresses that are obtained from the collapsed 3D empty model are set to zero in order to exclude the stresses and deformations. The numerical analysis algorithm for seismic analyses is shown in Figure 14.

Interaction elements should be defined between the dam body-foundation-concrete slab to provide interaction between the discrete surfaces. Special shear (k_s) and normal (k_n) stiffness coefficients are calculated according to the mechanical properties of each rockfill material in this study. These coefficients and special friction values are defined between these discrete surfaces to provide the interaction condition using the special fish functions. Normal-shear stiffness and friction values between the dam body and foundation are considered as 10^8 Pa/m and 30°, respectively. Moreover, it is considered 10^9 Pa/m for the concrete slab. While determining the boundary conditions of the 3D model, the special boundary conditions that are special for the nonlinear seismic analyses are used for the seismic analyses. Quiet boundary condition is defined for the bottom of the foundation to represent the viscous boundary condition. Moreover, the free-field boundary condition is used for the lateral surfaces of the 3D model. These important details are shown in Figure 15 in detail.

Accelerations and periods of the earthquakes are defined to the FLAC3D software using special fish functions, and these acceleration values are applied to the bottom of the 3D model considering x, y, and z directions of the earthquake. Characteristic properties of the earthquakes are shown in Table 2. As a result of the seismic analysis, the principal stresses are presented and assessed graphically for three critical nodal points on the dam body surface, and fatigue in the rockfill materials is evaluated in detail.

5.1. Principal Stress Results for Seismic Analyses. In this section, the effects of the far-fault earthquakes on the nonlinear principal stress behaviour of the Ilısu dam is examined in detail. Principal stress graphics and contour plot diagrams for principal stress results of the Ilısu dam are shown in Figures 16–22. Graphics represent the principal stress-time behaviour of the dam. Moreover, contour plots are created considering the maximum principal stress value that is acquired during the earthquake duration. Generally, the effects of each far-fault earthquake on the nonlinear

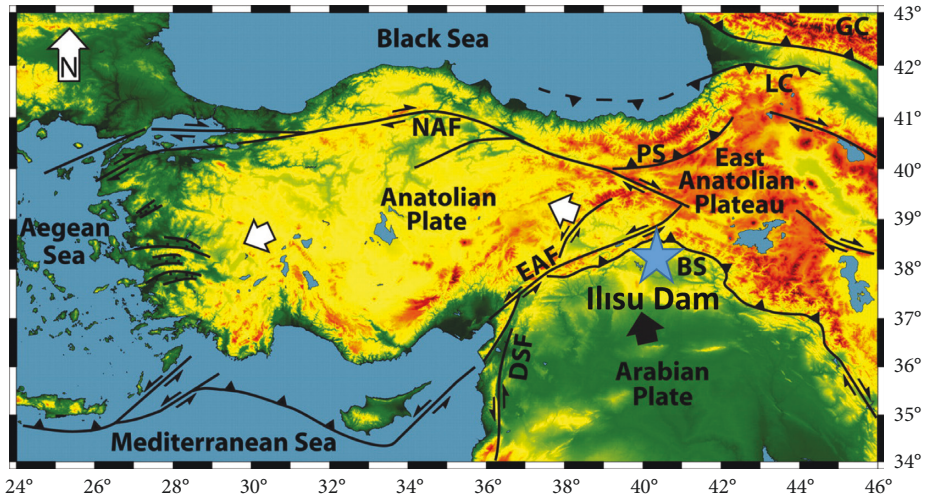

Figure 12: The fault map of Turkey and location of the Ilısu dam in seismic faults.

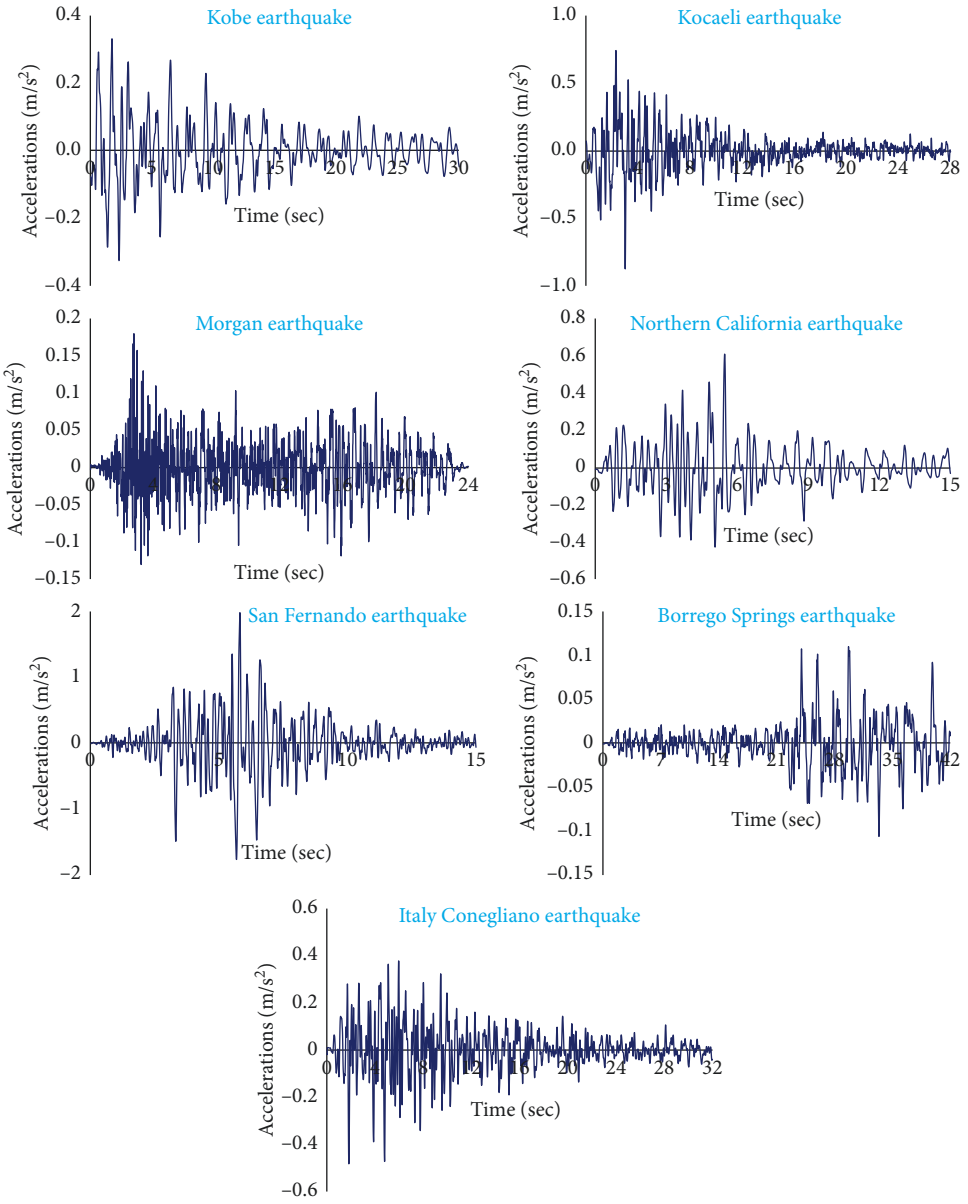

Figure 13: Acceleration-time graphics for 7 various far-fault earthquakes.

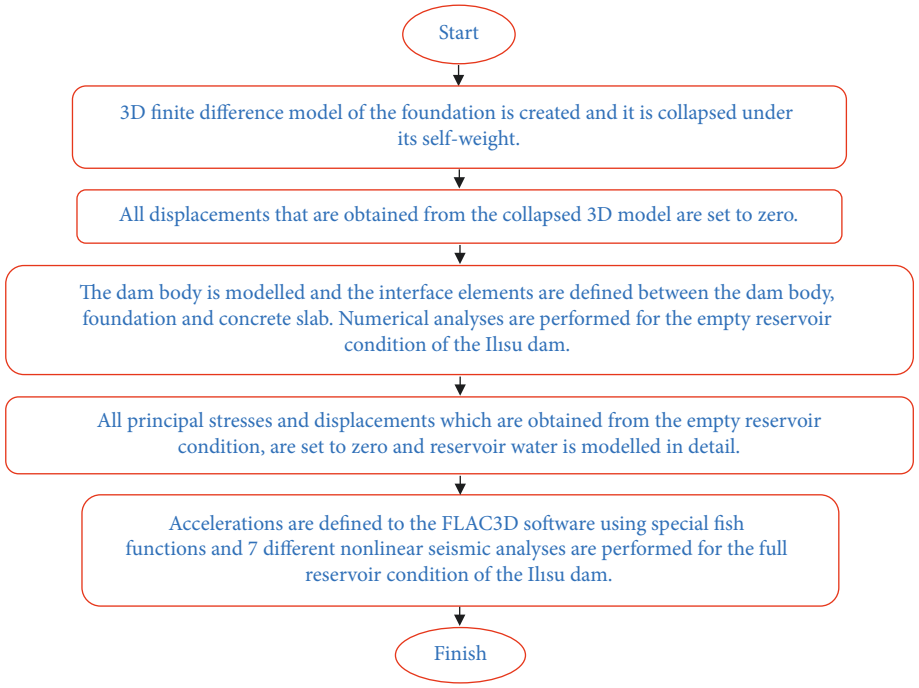

Figure 14: Numerical analysis algorithm for nonlinear seismic analyses.

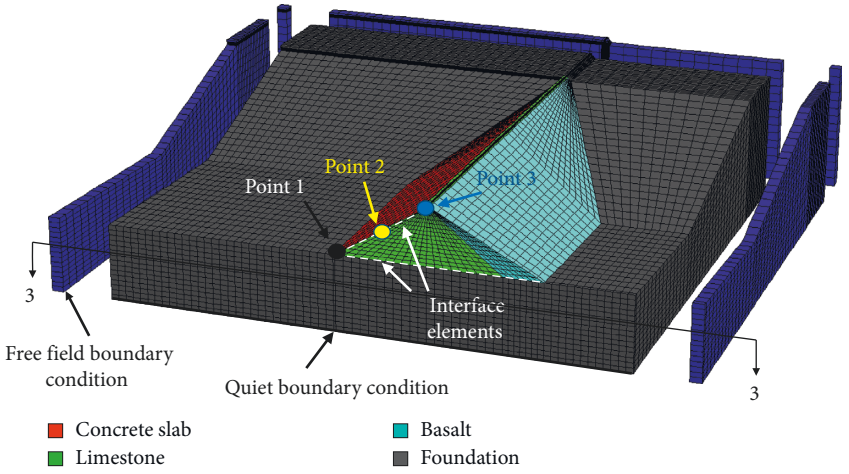

Figure 15: View from section 3-3 of the finite difference model of the Ilısu dam.

Table 2: Properties of the far-fault earthquakes.

Case	Earthquake	Time interval	Duration (sec)	A_p/V_p
Case 1	Borrego Springs	0.005	42	4.7
Case 2	Northern California	0.005	15	16.7
Case 3	Italy Conegliano	0.005	32	13.6
Case 4	Kobe	0.02	30	9.93
Case 5	Kocaeli	0.005	28	7.5
Case 6	Morgan	0.005	24	23.6
Case 7	San Fernando	0.01	15	18.5

principal stress behaviour of the dam are different from each other. This result obviously showed that various far-fault earthquakes create different fatigues in the rockfill materials of the dam. In addition, it is clearly seen from this result that various earthquake force has different stress effects on the nonlinear seismic behaviour of the Ilısu dam. The principal stress behaviour of the dam is observed taking into account 7 various far-fault earthquakes. Moreover, 3 important nodal points are selected from the dam body surface to better seen both the effect of hydrostatic pressure and nonlinear seismic effects on the nonlinear seismic behaviour of the dam. In Figures 16(a) and 16(b), principal stress results for Borrego earthquake are shown as graphical and plot contour diagram. It is clearly seen that maximum principal stress is obtained at 1.23th second of the earthquake (Figure 16(a)) and changes in the contour plot diagram for 1.23th second of the earthquake can be seen in Figure 16(b).

16.3 Mpa maximum principal stress occurred on the Point 1 (the lowest nodal point). Moreover, minimum stress

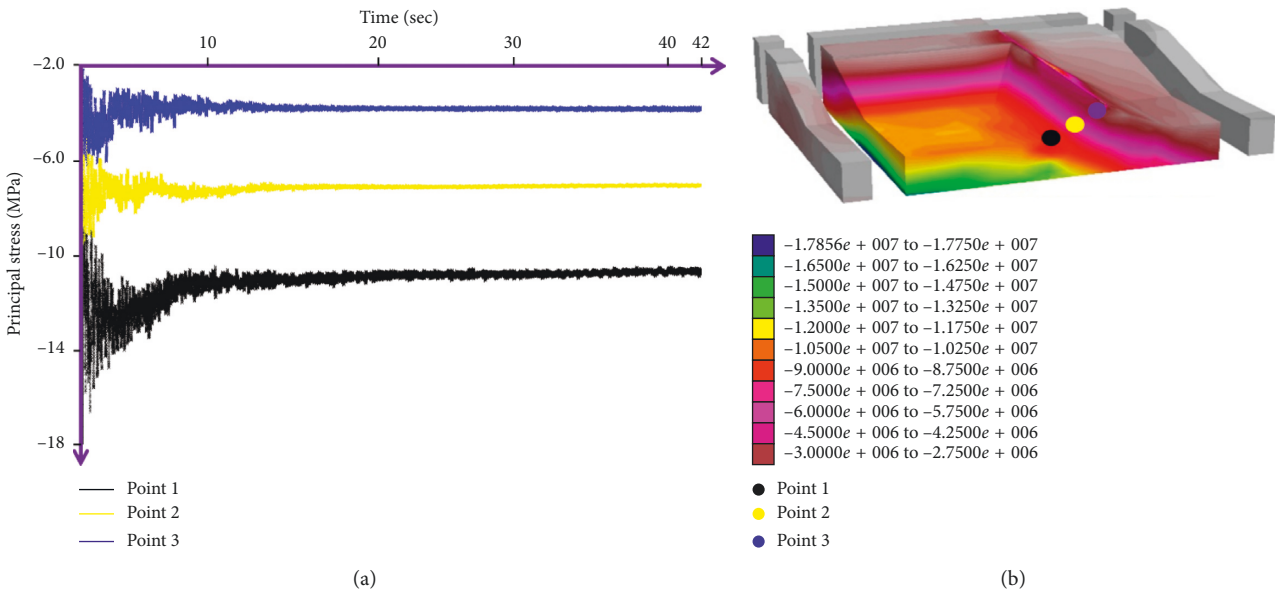

FIGURE 16: (a) Principal stress-time graphic for the Borrego earthquake. (b) Contour plot diagram for 42th second of the Borrego earthquake.

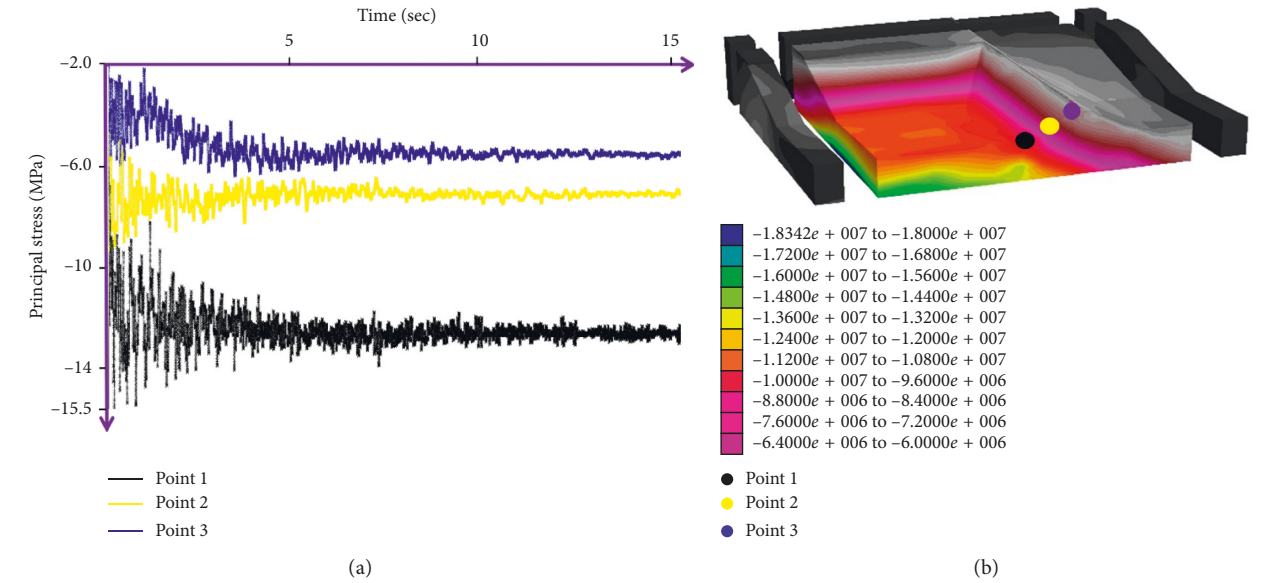

FIGURE 17: (a) Principal stress-time graphic for the California earthquake. (b) Contour plot diagram for 15th second of the California earthquake.

is observed on the Point 3 (top nodal point) as seen Figure 16(b). When examined Figures 17(a) and 17(b) (California earthquake stress results), 15.5 Mpa maximum principal stress value is observed on the Point 1 and minimum stress value is acquired on the Point 3. As clearly seen from Figure 17(b), direction of the water flowing is from upstream side of the dam to the downstream side. When compared Borrego and California earthquakes, it is obviously understood that different earthquakes create various seismic effects on the nonlinear principal stress behaviour of the dam.

According to Figures 18(a) and 18(b), the effect of Italy far-fault earthquake on the principal stress behaviour of the dam is clearly seen as graphical and contour plot diagram in detail. When compared 3 different nodal points, 14.26 Mpa maximum principal stress value occurred on the Point 1 and minimum stress value is observed on the Point 3 (Figure 18(a)). Maximum stress value is obtained at the 2nd second of the Italy earthquake. For this second of the earthquake, maximum principal stress value is 21.1 Mpa, and this value is acquired bottom of the foundation. No significant stresses are observed on the downstream surface of the dam body. This result clearly shows the effect of the hydrostatic pressure. Because of any external hydrostatic loads contact to these surfaces, any significant principal stress values are obtained on these surfaces. When examined

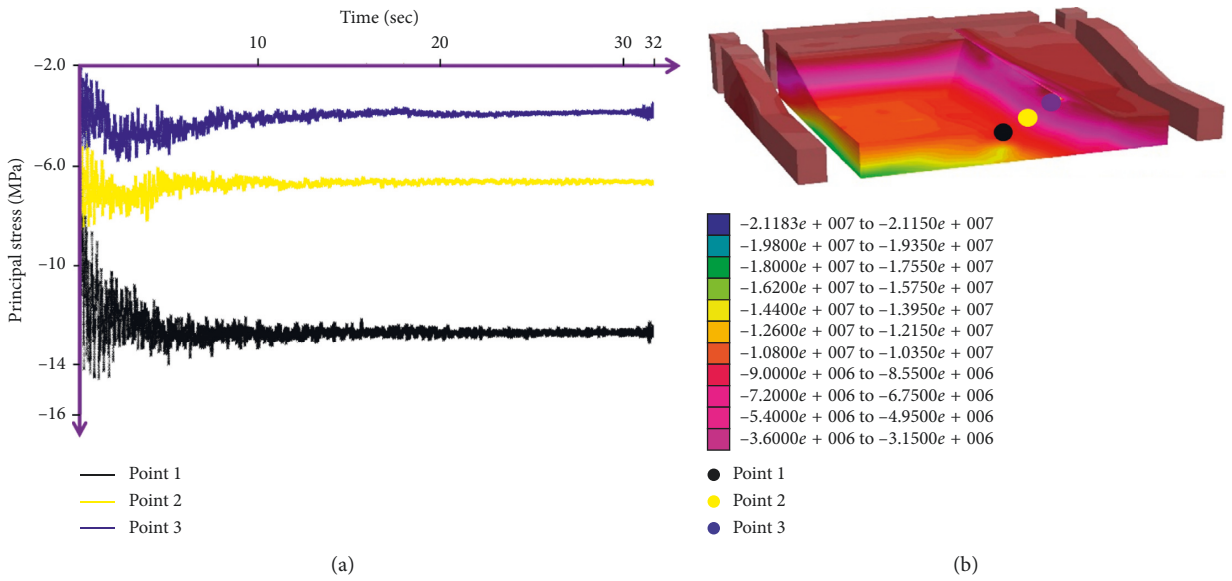

FIGURE 18: (a) Principal stress-time graphic for the Italy earthquake. (b) Contour plot diagram for 32nd second of the Italy earthquake.

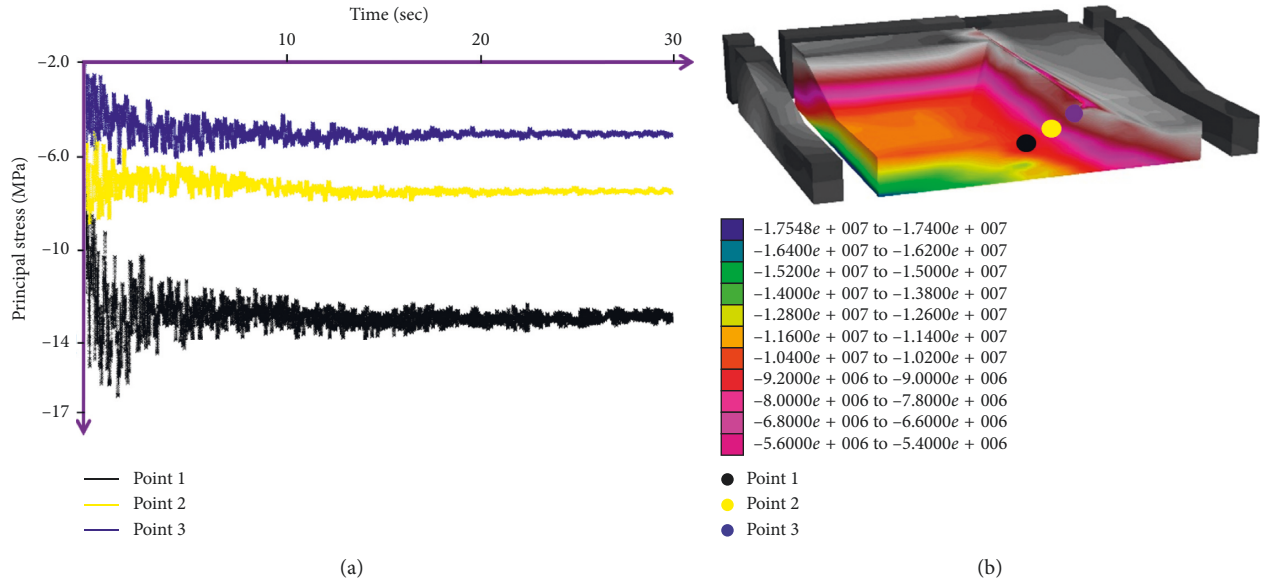

FIGURE 19: (a) Principal stress-time graphic for the Kobe earthquake. (b) Contour plot diagram for 30th second of Kobe earthquake.

the Kobe earthquake, 16.5 Mpa maximum principal stress value is observed on the Point 1 and minimum principal stress value occurred on the Point 3 as seen in Figure 19(a). This maximum value occurred at the 3rd second of the Kobe earthquake. The contour plot diagram for this second of the earthquake is presented in Figure 19(b). 17.54 Mpa maximum stress value is obtained at the bottom of the foundation. Moreover, direction of the water flowing in the dam body is clearly seen from Figure 19(b).

According to the effect of the Kocaeli far-fault earthquake on the nonlinear principal stress behaviour of the dam, approximately 18 Mpa maximum principal stress value is observed on the Point 1, and minimum stress value occurred on the Point 3 when compared 3 various nodal points (Figure 20(a)). During the 28th second of the Kocaeli earthquake, 27.73 Mpa maximum principal stress value is observed at the bottom of the 3D model and minimum principal stress values occurred at the downstream surfaces of the dam because of any external water pressure contact to the downstream side of the dam body surface (Figure 20(b)). When investigated the Morgan far-fault earthquake, 14.91 Mpa maximum principal stress value is observed on the Point 1 at the 2nd second of the earthquake. Moreover, minimum stress value is obtained on the Point 1 as seen Figure 21(a). Contour plot diagrams for this second are shown in Figure 21(b) in detail. During the Morgan earthquake, the maximum stress value, 25.96 Mpa, is observed at bottom of the foundation. Significant principal

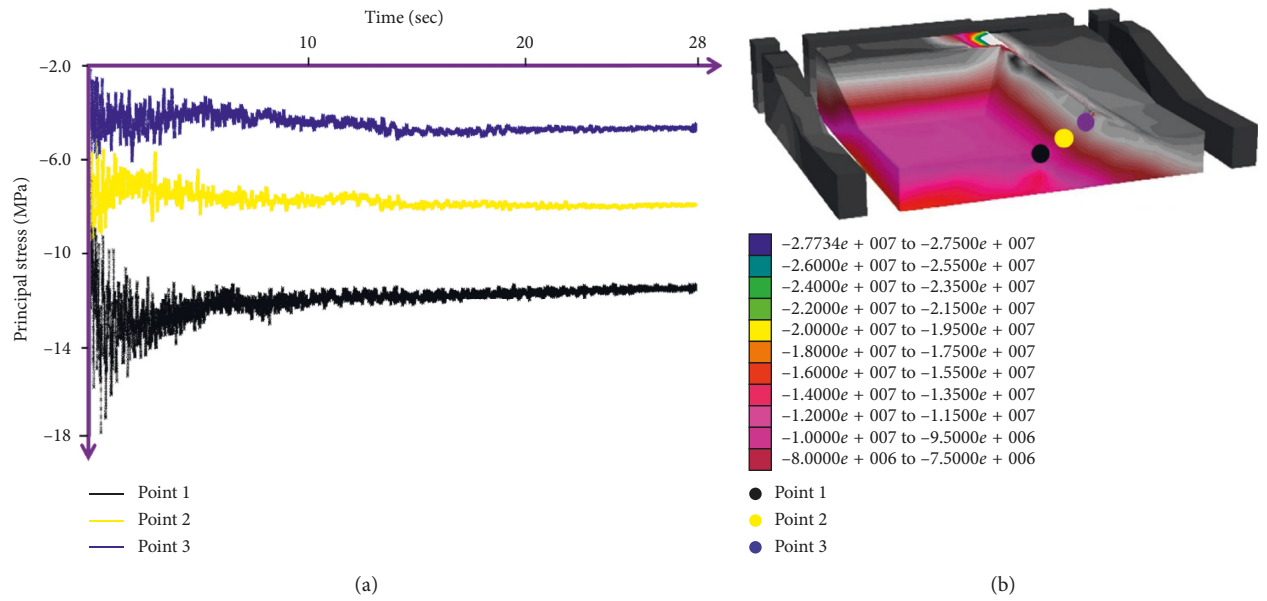

FIGURE 20: (a) Principal stress-time graphic for the Kocaeli earthquake. (b) Contour plot diagram for 28th second of the Kocaeli earthquake.

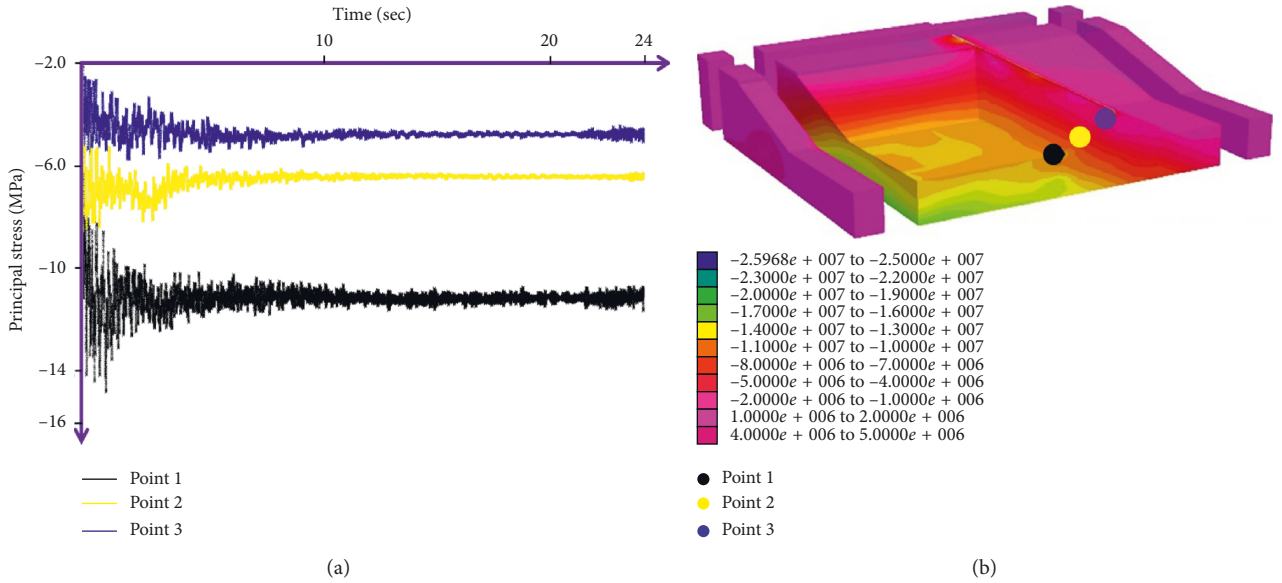

FIGURE 21: (a) Principal stress-time graphic for the Morgan earthquake. (b) Contour plot diagram for 24th second of the Morgan Earthquake.

stress values are obtained at the upstream side of the foundation surface. In addition, any stress values are observed at the downstream surfaces of the foundation. This result obviously indicated the effect of the hydrostatic pressure on the nonlinear seismic stress behaviour of the dam. According to San Fernando earthquake, 14.83 Mpa maximum principal stress value is observed on the Point 1 and minimum stress value occurred on the Point 3 (Figure 22(a)). Maximum principal stress value occurred at the 1.6th second of the earthquake. For this second, stress values are shown in Figure 22(b) in detail. The maximum stress value, 18.28 Mpa, is observed at bottom of the foundation for this second. Moreover, a principal stress value of approximately 11 Mpa is observed on the surface of the dam body as shown in Figure 22(b).

6. Conclusion

In this paper, the nonlinear seismic behaviour of the Ilısu dam is examined for various far-fault earthquakes considering the dam body-foundation-concrete slab interaction condition and special seismic boundary conditions. These boundary conditions are free-field and quiet boundary conditions, and they were rarely used for the seismic analysis of the CFR dams in the past. The three-dimensional (3D) finite difference model of the Ilısu dam is modelled using the

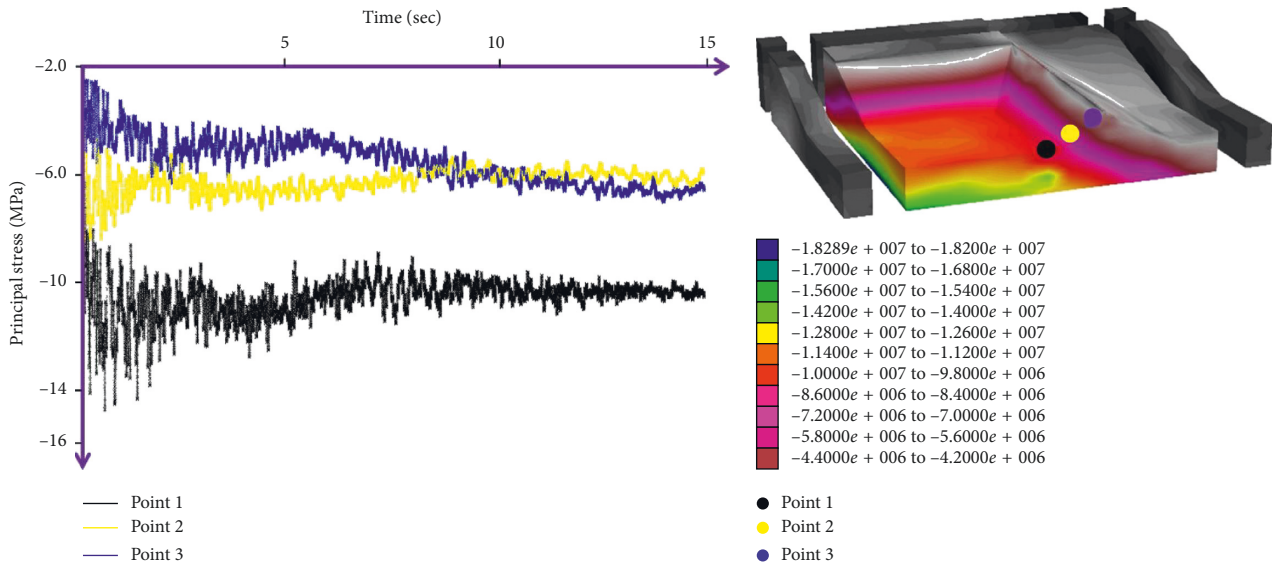

FIGURE 22: (a) Principal stress-time graphic for the San Fernando earthquake. (b) Contour plot diagram for 15th second of the San Fernando earthquake.

special fish functions, and it is created according to the original dam project. While creating the 3D model, Mohr–Coulomb and Drucker–Prager nonlinear material models are used for the rockfill materials and concrete slab, respectively. While performing the seismic analyses, earthquake accelerations are applied to the bottom of the 3D model using special fish functions. Totally 7 different far-fault earthquakes are taken into account for the seismic analyses. Therefore, total 7 various nonlinear earthquake analyses are performed for the full-reservoir conditions of the Ilısu dam. The effects of these far-fault ground motions on the nonlinear earthquake behaviour of the Ilısu dam are evaluated as follows:

(i) When comparing the upstream and downstream sides of the dam, significant principal stress differences are observed by the effect of hydrostatic water pressure. According to all seismic analysis results, more principal stresses are observed on the upstream surfaces of the dam.

(ii) According to 7 various far-fault earthquake analyses, maximum principal stress on the dam body surface is observed for Kocaeli far-fault earthquake on Point 1, and its numerical value is 18 Mpa. This result is very significant for evaluating of seismic behaviour of CFR dams.

(iii) The effect of the free-field and quiet boundary conditions that were rarely used for seismic analyses in the past on the seismic behaviour of CFR dams is clearly seen in this study. It is observed that these nonreflecting seismic boundary conditions could be used for modelling and analyzing the CFR dams.

(iv) Far-fault earthquakes create different seismic stress effects on each nodal point of the dam body. These effects may be very critical on the earthquake behaviour of CFR dams. In this study, the effect of far-fault earthquakes on the nonlinear seismic behaviour of the Ilısu dam is clearly seen, and each far-fault earthquake caused various significant principal stresses on each nodal points of this dam.

(v) According to the nonlinear seismic analysis results, maximum principal stress occurred on the lowest nodal point (Point 1) and minimum stress is observed on the top nodal point (Point 3). This result clearly shows the effect of the hydrostatic pressure and far-fault earthquake loads on the nonlinear seismic stress behaviour of the Ilısu CFR dam.

Conflicts of Interest

The authors declare that they have no conflicts of interest.

References

[1] T. Z. Yeow, G. A. MacRae, and R. P. Dhakal, "Wall building stiffness and strength effect on content sliding in Wellington seismic conditions," *Earthquake Eng. & Structural dynamics*, vol. 46, no. 6, pp. 1023–1042, 2016.

[2] D. E. Hudson, *The Wilmont Survey Type Strong-Motion Earthquake Recorder*, Earthquake Engineering Research Laboratory, California Institute of Technology, Pasadena, CA, USA, 1958.

[3] G. W. Housner and M. D. Trifunac, "Analysis of accelerograms--Parkfield earthquake," *Bulletin of the Seismological Society of America*, vol. 57, pp. 1193–1220, 1967.

[4] H. M. Westergaard, "Water pressures on dams during earthquakes," *Transactions of the American Society of Civil Engineers*, vol. 98, no. 2, pp. 418–433, 1933.

[5] A. K. Chopra, "Hydrodynamic pressures on dams during earthquakes, Berkeley," Structures and Materials, Report No. 66-2A. University of California Berkeley, Berkeley, CA, USA, 1966.

[6] Y. Arici, "Evaluation of the performance of the face slab of a CFRD during earthquake excitation," *Soil Dynamics and Earthquake Engineering*, vol. 55, pp. 71–82, 2013.

[7] X.-g. Yang and S.-c. Chi, "Seismic stability of earth-rock dams using finite element limit analysis," *Soil Dynamics and Earthquake Engineering*, vol. 64, pp. 1–10, 2014.

[8] K. I. Andrianopoulos, A. G. Papadimitriou, G. D. Bouckovalas, and D. K. Karamitros, "Insight into the seismic response of earth dams with an emphasis on seismic coefficient estimation," *Computers and Geotechnics*, vol. 55, pp. 195–210, 2014.

[9] B. Xu, D. Zou, X. Kong, Z. Hu, and Y. Zhou, "Dynamic damage evaluation on the slabs of the concrete faced rockfill dam with the plastic-damage model," *Computers and Geotechnics*, vol. 65, pp. 258–265, 2015.

[10] W.-J. Cen, L.-S. Wen, Z.-Q. Zhang, and K. Xiong, "Numerical simulation of seismic damage and cracking of concrete slabs of high concrete face rockfill dams," *Water Science and Engineering*, vol. 9, no. 3, pp. 205–211, 2016.

[11] B. Han, L. Zdravkovic, S. Kontoe, and D. M. G. Taborda, "Numerical investigation of the response of the Yele rockfill dam during the 2008 Wenchuan earthquake," *Soil Dynamics and Earthquake Engineering*, vol. 88, pp. 124–142, 2016.

[12] D. Zou, H. Han, J. Liu, D. Yang, and X. Kong, "Seismic failure analysis for a high concrete face rockfill dam subjected to near-fault pulse-like ground motions," *Soil Dynamics and Earthquake Engineering*, vol. 98, pp. 235–243, 2017.

[13] Y. Yazdani and M. Alembagheri, "Seismic vulnerability of gravity dams in near-fault areas," *Soil Dynamics and Earthquake Engineering*, vol. 102, pp. 15–24, 2017.

[14] A. Bayraktar and M. E. Kartal, "Linear and nonlinear response of concrete slab on CFR dam during earthquake," *Soil Dynamics and Earthquake Engineering*, vol. 30, pp. 990–1003, 2010.

[15] R. Noorzad and M. Omidvar, "Seismic displacement analysis of embankment dams with reinforced cohesive shell," *Soil Dynamics and Earthquake Engineering*, vol. 30, pp. 1149–1157, 2010.

[16] A. R. Khoei and T. Mohammadnejad, "Numerical modeling of multiphase fluid flow in deforming porous media: a comparison between two- and three-phase models for seismic analysis of earth and rockfill dams," *Computers and Geotechnics*, vol. 38, pp. 142–166, 2011.

[17] A. Seiphoori, S. Mohsen Haeri, and M. Karimi, "Three-dimensional nonlinear seismic analysis of concrete faced rockfill dams subjected to scattered P, SV, and SH waves considering the dam-foundation interaction effects," *Soil Dynamics and Earthquake Engineering*, vol. 31, pp. 792–804, 2011.

[18] A. Bayraktar, M. E. Kartal, and S. Adanur, "The effect of concrete slab-rockfill interface behavior on the earthquake performance of a CFR dam," *International Journal of Non-Linear Mechanics*, vol. 46, pp. 35–46, 2011.

[19] Y. Yamaguchi, M. Kondo, and T. Kobori, "Safety inspections and seismic behavior of embankment dams during the 2011 off the Pacific Coast of Tohoku earthquake," *Soils and Foundations*, vol. 52, no. 5, pp. 945–955, 2012.

[20] P. Dakoulas, "Nonlinear seismic response of tall concrete-faced rockfill dams in narrow canyons," *Soil Dynamics and Earthquake Engineering*, vol. 34, pp. 11–24, 2012.

[21] X. Kong, Y. Zhang, D. Zou, Y. Qu, and X. Yu, "Seismic cracking analyses of two types of face slab for concrete-faced rockfill dams," *Science China Technological Sciences*, vol. 60, no. 4, pp. 510–522, 2017.

[22] D. Zou, B. Xu, X. Kong, H. Liu, and Y. Zhou, "Numerical simulation of the seismic response of the Zipingpu concrete face rockfill dam during the Wenchuan earthquake based on a generalized plasticity model," *Computers and Geotechnics*, vol. 49, pp. 111–122, 2013.

[23] H. Xu, D. Zou, X. Kong, Z. Hu, and X. Su, "A nonlinear analysis of dynamic interactions of CFRD-compressible reservoir system based on FEM-SBFEM," *Soil Dynamics and Earthquake Engineering*, vol. 112, pp. 24–34, 2018.

[24] B. Xu, Y. Zhou, and D. Zou, "Numerical simulation on slabs dislocation of Zipingpu concrete faced rockfill dam during the Wenchuan earthquake based on a generalized plasticity model," *Scientific World Journal*, vol. 2014, Article ID 572407, 5 pages, 2014.

[25] DSI, *General Directorate of State Hydraulic Works*, Regional Directorate, Ankara, Turkey, 2018.

[26] Itasca Consulting Group, Inc., *FLAC Version 5 User Manual*, Itasca Consulting Group, Inc., Minneapolis, MN, USA, 2002.

[27] M. Karalar and M. Çavuşli, "Effect of normal and shear interaction stiffnesses on three-dimensionalviscoplastic creep behaviour of a CFR dam," *Advances in Civil Engineering*, vol. 2018, Article ID 2491652, 2018.

[28] M. E. Kartal, M. Cavusli, and A. B. Sunbul, "Assessing seismic response of a 2D roller-compacted concrete dam under variable reservoir lengths," *Arabian Journal of Geoscience*, vol. 10, no. 22, p. 488, 2017.